# Imaging spatio-temporal Hong-Ou-Mandel interference of bi-photon states of extremely high Schmidt number

Fabrice Devaux[1*], Alexis Mosset[1], Paul-Antoine Moreau[2], and Eric Lantz[1]
[1] *Institut FEMTO-ST, Département d'Optique P. M. Duffieux, UMR 6174 CNRS Université Bourgogne Franche-Comté, 15b Avenue des Montboucons, 25030 Besançon, France and*
[2] *School of Physics and Astronomy, University of Glasgow, G12 8QQ, UK**
(Dated: November 29, 2023)

We report the experimental observation of a spatio-temporal Hong-Ou-Mandel (HOM) interference of bi-photon states of extremely high Schmidt number. Two-photon interference of 1500 spatial modes and a total of more than $3 \times 10^6$ spatio-temporal modes is evidenced by measuring momentum spatial coincidences between the pixels of the far-field images of two strongly multimode spontaneous parametric down conversion (SPDC) beams propagating through a HOM interferometer. The outgoing SPDC beams are recorded onto two separate detectors arrays operating in the photon-counting regime. The properties of HOM interference are investigated both in the time and space domains. We show that the two-photon interferences exhibit temporal and two-dimensional spatial HOM dips with visibilities of 30% and widths in good agreement with the spatio-temporal coherence properties of the bi-photon state. Moreover, we demonstrate that a peak of momentum spatial coincidences is evidenced inside each image, in correspondence with this dip.



## I. INTRODUCTION

Spatial entanglement of photon pairs in images offers new opportunities to develop protocols for communication and parallel treatment of quantum informations of potentially very high dimensionality. Although entangled photon pairs of high Schmidt number are easily produced by SPDC, the manipulation and the detection of images with quantum features is tricky. Fortunately, detector arrays with high sensitivity such as Electron Multiplying Coupled-Charge Device (EMCCD), intensified charge coupled device (iCCD) or single photon avalanche diode (SPAD) array [1] are now widely used for quantum imaging experiments [2] like demonstration of Einstein-Podolsky-Rosen (EPR) paradox in twin images [3, 4], ghost imaging [5, 6], quantum adaptive optics [7], quantum holography [8], sub-shot-noise imaging [9, 10] and quantum imaging with undetected photons [11].

Among the whole experiments using entangled pairs of photons, the famous experiment of two-photon interference known now as Hong-Ou-Mandel (HOM) interference [12], is probably one of the most fascinating. This groundbreaking experiment paved the way for a multitude of experiments showing the richness of the quantum properties of SPDC and their application to original communication protocols [13]. Most of these experiments and protocols used the coherence time property of the bi-photon state and the measurements of the quantum properties are performed by means of bucket detectors and coincidence counters gated in time. HOM interference is obtained if the two involved photons are indistinguishable, whatever their origin, meaning that extremely dissimilar light sources [14] can be used if the corresponding modes are thoroughly tailored. On the other hand, genuine multi-mode HOM interference implies entanglement, as quoted by Lee et al [15], and SPDC remains the simplest way to produce entangled photon pairs of high dimensionality. Recently, Jachura et al. [16] extended the applications of the camera systems to the observation of HOM interference with an intensified scientific complementary metal-oxide-semiconductor (sCMOS) camera, showing a maximum of coincidences on the same region of interest (ROI) of the camera in conditions corresponding to a minimum of the dip between separate ROI of the camera. Nevertheless, the input photons were spatially filtered by traversing a single-mode fiber to ensure an unique input spatial mode for each photon. It is possible to imprint a phase profile on one of the photon and to realize its hologram, as demonstrated by the same group [17]. Also in this experiment, an only spatial mode per input port is involved, even if shaped. In the experiments reported in Refs [18, 19], it was shown that a tilt between the spatially monomode input beams results in coincidence fringes, that were detected by scanning a bucket detector. On the other hand, two experiments demonstrated multi-mode HOM interference. First, Walborn et al. [20] showed that a HOM dip can be transformed in a HOM peak by using either

*Corresponding author:fabrice.devaux@univ-fcomte.fr

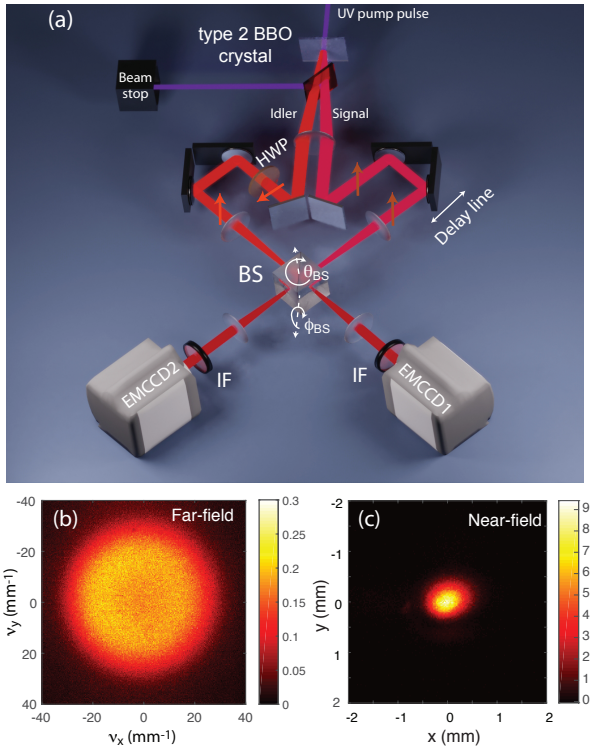


FIG. 1: (a) Experimental setup. (b) and (c) average images in photon number of the far-field and the near-field of a single SPDC beam, respectively.

an antisymmetric pump beam or an antisymmetric polarization vector of the entangled photon pair. Second, Lee et al [15] employed bucket detectors and time coincidence to characterize HOM interference from SPDC limited by an aperture, resulting in a maximum of about 40 spatial modes.

Recently, using numerical simulations with realistic parameters, we have shown how two cameras can be used to detect two-dimensional (2D) spatial coincidences of bi-photon states of high dimensionality and to evidence HOM interferences between the two outgoing images [21]. Thank to this numerical model, we have demonstrated that such a HOM interferometer allows the characterization of the temporal as well as the 2D spatial coherence properties of entangled photons pairs. In this paper, we report the first experimental observation of a fully spatio-temporal HOM interference of bi-photon states of high Schmidt number. Two-photon interferences are evidenced by measuring the 2D momentum spatial coincidences between the pixels of far-field images of twin SPDC beams propagating through the HOM interferometer. The images are recorded onto two EMCCDs operating in the photon-counting regime [22]. The use of EMCCDs allows the detection of all photons of the images and the measurement of spatial coincidences on the whole set of photons.The properties of HOM interference are investigated both in the time and space domains, as it was proposed in [21].

## II. EXPERIMENTAL SETUP AND METHOD

Fig. 1a shows the experimental setup. Strongly multimode twin SPDC beams (i.e. bi-photon states of high Schmidt number) are generated in a noncolinear type-II geometry in a $0.8\,mm$ long $\beta$-barium borate ($\beta$-BBO) crystal pumped at $355\,nm$. The pump pulses are provided by a passively Q-switched Nd:YAG laser ($\Delta t_{pump} = 660\,ps$ FWHM pulse duration, 8 $mW$ mean power and 4 $kHz$ repetition rate). Because of the noncolinear interaction, the twin beams are separated and propagate through the two input ports of the HOM interferometer up to a beamsplitter (BS: $R$=50%, $T$=40%, losses 10%). In both arms, two identical 1.5 magnification telescopes form the near-field images of the BBO crystal inside the BS. Because of the geometry of the interferometer [21] where SPDC beams propagate in the horizontal plane, the reflected beams experience a left-right symmetry with respect to the transmitted beams in the near-field as well as in the far-field. Before the BS, the polarization state of the idler beam is controlled with a half-wave plate (HWP), in order to measure spatial correlations when the polarizations states of the twin photons are horizontal-vertical ($HV$) or vertical-vertical ($VV$). Then, the far-field of the two outgoing images is formed

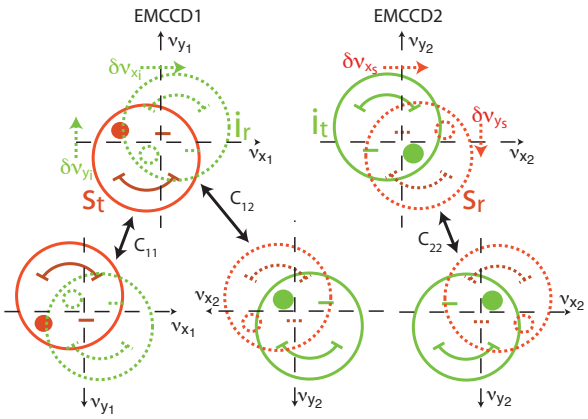


FIG. 2: Diagrams illustrating, on both cameras, the relative positions of the far-field patterns of the signal and idler beams when they are either transmitted ($s_t$, $i_t$) or reflected ($s_r$, $i_r$) as a function of the shifts $\delta\nu_{x_i} = \delta\nu_{x_s}$ and $\delta\nu_{y_i} = -\delta\nu_{y_s}$ induced by horizontal and vertical tilts of the BS, respectively. The solid and dotted line circles correspond to the transmitted beams and to the reflected beams, respectively. The origins of the axes are centered on the barycenters of the images. Spatial correlations can be observed inside images symmetrically to the horizontal axes ($C_{11}$ and $C_{22}$) and between images symmetrically to the images barycenters ($C_{12}$).

with $2f$ imaging systems on two separate EMCCDs (ANDOR iXon Ultra 897), used in photon-counting regime [22]. Before detection, the photons pairs emitted around the degeneracy are selected by narrow-band interference filters (IF) centered at $709\,nm$ ($\Delta\lambda_{IF} \backsimeq 5\,nm$, FWHM bandwidth). Figures 1b and 1c show typical far-field and near-field average images of the SPDC beams through the HOM interferometer. The axes of the far-field image are graduated in spatial frequency coordinates $\nu_{x,y}$, which are related to momentum coordinates by $q_{x,y} = 2\pi\nu_{x,y}$.

The control, by a delay line, of the time delay $\delta t$ between the input ports of the HOM interferometer gives access to the coherence length. Meanwhile, the control of a 2D transverse spatial frequency shift between the transmitted and reflected beams at the output ports, by the rotations $\delta\theta_{BS}$ and $\delta\phi_{BS}$ of the BS, gives access to the two transverse coherence widths of the bi-photon states. From the far-field and near-field images of the SPDC beams (figures 1b and 1c), the time duration of the pump pulse and the bandwidth of the IF, we estimate the standard deviations of the SPDC beams in the spatial and temporal domains as:

$$\begin{cases} \sigma_x^{SPDC} \simeq \sigma_x^{pump} \simeq 0.35\,mm \\ \sigma_y^{SPDC} \simeq \sigma_y^{pump} \simeq 0.37\,mm \\ \sigma_{\nu_x}^{SPDC} \simeq 34\,mm^{-1} \\ \sigma_{\nu_y}^{SPDC} \simeq 34\,mm^{-1} \\ \sigma_t^{SPDC} \simeq \sigma_t^{pump} \simeq 400\,ps \\ \sigma_{\nu_t}^{SPDC} \simeq \sigma_{\nu_t}^{IF} \simeq 1.8\,THz \end{cases} \tag{1}$$

Using the definition of the Schmidt number [23] along the dimension $i$ (where $i = x, y, t$): $K_i = \frac{1}{2}\left(\sigma_i^{pump} 2\pi\sigma_{\nu_i}^{SPDC} + \frac{1}{\sigma_i^{pump} 2\pi\sigma_{\nu_i}^{SPDC}}\right)$, we have estimated the Schmidt numbers for each dimension:

$$\begin{cases} K_x \simeq 37 \\ K_y \simeq 40 \\ K_t \simeq 2.3 \times 10^3 \end{cases} \tag{2}$$

Finally, the full space-time dimensionality of the bi-photon states can be estimated as $K_x K_y K_t \simeq 3.4 \times 10^6$ which confirms the extremely high dimensionality of the twin photons involved in the HOM interference.

Fig. 2 illustrates schematically the relative positions and orientations of the far-field patterns of the SPDC beams, when they are either transmitted or reflected by the BS. Because of the geometry of the HOM interferometer [21], horizontal and vertical tilts of the BS induce momenta shifts $\boldsymbol{\delta q}$ of the reflected beams which are related to 2D spatial frequency shifts $\delta\nu_{x_i} = \delta\nu_{x_s} = 2f\delta\theta_{BS}$ and $\delta\nu_{y_i} = -\delta\nu_{y_s} = 2f\delta\phi_{BS}$, where $f$ is the focal length of the last lenses before the EMCCDs. Using detectors arrays, the momentum spatial correlations between the photons of a pair can be measured between images for transmitted-transmitted ($tt$) and reflected-reflected ($rr$) twin photons and also inside single images for reflected-transmitted ($rt$) and transmitted-reflected ($tr$) twin photons. These different kinds of spatial correlations between photons of pairs can be observed in Fig. 2.

First, let us consider the case where the transmitted and reflected beams are perfectly superimposed on both cameras ($\boldsymbol{\delta q} = \mathbf{0}$), perfectly synchronized ($\delta t = 0$) and parallely polarized (VV configuration). For both reflected ($rr$) and transmitted beams ($tt$), momentum correlations are found between pixels of the two cameras corresponding to opposite transverse momenta coordinates $\boldsymbol{q_1}$ and $\boldsymbol{q_2} = -\boldsymbol{q_1} + \boldsymbol{\Delta q}$, where $\boldsymbol{\Delta q}$ denotes the 2D momentum correlation uncertainty. By calculating the normalized cross-correlation between the image 1 and the up-down and left-right symmetric image 2, we will obtain the spatial distribution of the momentum correlations as a function of the 2D momentum uncertainty : $C_{12}(\boldsymbol{\Delta q})$ . For the $rt$ and $tr$ beams, momentum correlations are found inside each image between the pixels symmetric with respect to the horizontal axis, corresponding to transverse momenta coordinates ($q_{x1}$, $q_{y1}$) and ($q_{x1} + \Delta q_x$, $-q_{y1} + \Delta q_y$) for camera 1 and ($q_{x2}$, $q_{y2}$) and ($q_{x2} + \Delta q_x$, $-q_{y2} + \Delta q_y$) for camera 2. For each image, measurements are performed by calculating the normalized cross-correlation between the upper half and the up-down symmetric lower half parts of single images. In that case, we do not perform the correlation calculation on the whole image because the correlations between twin photons detected on the same camera would be counted twice. Then, we obtain the spatial distributions of the momentum correlations inside each image as a function of the 2D momentum uncertainty : $C_{11}(\boldsymbol{\Delta q})$ and $C_{22}(\boldsymbol{\Delta q})$. In all cases, the correlation distributions have the shape of 2D gaussian functions with standard deviations related to the spatial dimensionality of the bi-photon states. Now, let us consider the case where a time delay and a momentum shift are imposed. In that case, using the formalism proposed in [21] and [12], we can establish the relations that give the spatial distributions of momentum correlations as a function of $\delta t$ and $\boldsymbol{\delta q}$:

$$\begin{cases} C_{12}\left(\boldsymbol{\Delta q}; \delta t, \boldsymbol{\delta q}\right) = \\ \left[R^2 C_0\left(\boldsymbol{\Delta q} + \boldsymbol{\delta q_x}\right) + T^2 C_0\left(\boldsymbol{\Delta q} - \boldsymbol{\delta q_x}\right)\right] \times \\ \left(1 - \dfrac{2RT}{R^2+T^2} e^{-\frac{\delta q_x^2}{\sigma_q^2}} e^{-\frac{\delta q_y^2}{\sigma_{SPDC}^2}} e^{-\frac{\delta t^2}{\sigma_t^2}}\right) \\ C_{11}\left(\boldsymbol{\Delta q}; \delta t, \boldsymbol{\delta q}\right) + C_{22}\left(\boldsymbol{\Delta q}; \delta t, \boldsymbol{\delta q}\right) = \\ RT\left[C_0\left(\boldsymbol{\Delta q} + \boldsymbol{\delta q_x}\right) + C_0\left(\boldsymbol{\Delta q} - \boldsymbol{\delta q_x}\right)\right] \times \\ \left(1 + e^{-\frac{\delta q_x^2}{\sigma_q^2}} e^{-\frac{\delta q_y^2}{\sigma_{SPDC}^2}} e^{-\frac{\delta t^2}{\sigma_t^2}}\right) \end{cases} \tag{3}$$

$C_0(\boldsymbol{\Delta q})$ is the spatial distribution of momentum correlations measured between twin images when the BS is removed. According to these equations, we should measure two correlation peaks centered along the horizontal axis at a distance related to the horizontal spatial shift and with amplitudes related to the spatial and temporal shifts. As it was demonstrated in [21], the standard deviations of the spatial HOM dip depend of the coherence width of the bi-photon wave-packet along the horizontal dimension $\sigma_q$ and of the phase matching bandwidth $\sigma_{SPDC}$ along the vertical dimension. $\sigma_t$ is the standard deviation of the temporal HOM dip. A 2D space integration of the equations 3, normalized by a 2D space integration of $C_0(\boldsymbol{\Delta q})$, leads to the relative spatial correlations as a function of the momentum shift and the time delay as follows:

$$\begin{cases} R_{12}(\delta t, \boldsymbol{\delta q}) = R^2 + T^2 - 2RT e^{-\frac{\delta q_x^2}{\sigma_q^2}} e^{-\frac{\delta q_y^2}{\sigma_{SPDC}^2}} e^{-\frac{\delta t^2}{\sigma_t^2}} \\ R_{11}(\delta t, \boldsymbol{\delta q}) + R_{22}(\delta t, \boldsymbol{\delta q}) = \\ 2RT \times \left(1 + e^{-\frac{\delta q_x^2}{\sigma_q^2}} e^{-\frac{\delta q_y^2}{\sigma_{SPDC}^2}} e^{-\frac{\delta t^2}{\sigma_t^2}}\right) \end{cases} \tag{4}$$

With $R$=50% and $T$=40%, the expected visibilities of $R_{12}$ and $R_{11} + R_{22}$ are 95% and 33%, respectively.

## III. EXPERIMENTAL RESULTS

### A. Temporal coherence measurements

The first experiment consists in measuring the temporal coherence of the bi-photon states. To this end, the signal and the idler beams are spatially superimposed at best in the near-field and in the far-field domains. Then, spatial momentum correlations are measured, between pairs of images as well as inside single images, as a function of the optical path delay between the two arms of the HOM interferometer and as a function of the polarization states $HV$ and $VV$ of the twin photons. Fig. 3 shows the spatial momentum correlations distributions obtained when they are measured between image pairs ($C_{12}$) and inside single images ($C_{11}$, $C_{22}$) and when the time delay between the two

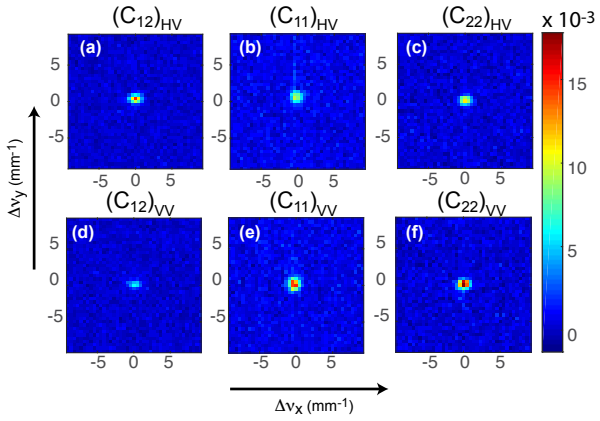


FIG. 3: Average normalized spatial momentum correlations distributions obtained when correlations are measured between image pairs ($C_{12}$) and inside single images ($C_{11}$, $C_{22}$) when the optical paths difference between the two arms of the interferometer is null. $HV$ and $VV$ indices are related to the polarization states of the twin photons.

arms of the interferometer is null. These results are averaged over 500 pairs of images. Figures 3a to 3c are related to the $VV$ polarization states and figures 3d to 3f to the $HV$ polarization states. From these figures, we can observe that the three correlation peaks have the same gaussian-like shapes with standard deviations $\sigma_{\nu_x} = 0.8 \pm 0.2\, mm^{-1}$ and $\sigma_{\nu_y} = 0.6 \pm 0.2\, mm^{-1}$. It means that spatial momentum correlations are measured with the same precision between images or inside single images. Then, we can roughly estimate the spatial dimensionality of the bi-photon states as $\frac{\sigma_{\nu_x}^{SPDC}\sigma_{\nu_y}^{SPDC}}{\sigma_{\nu_x}\sigma_{\nu_x}} = \frac{34^2}{0.8 \times 0.6} \backsimeq 2400$. This result is consistent with the estimated $K_x$ and $K_y$ Schmidt numbers (Eq. 2) and confirms the high spatial dimensionality of the bi-photon states. By integrating the correlation peaks, we have estimated the ratio of the events corresponding to the detection of photons by pairs between images and inside single images. When twin photons are cross-polarized ($HV$), these ratios are $13 \pm 2\%$ in $C_{12}$ and $7 \pm 1\%$ in $C_{11}$ and $C_{22}$. It means that more or less half of the spatial momentum coincidences are recorded between the two images and the other half is equally distributed inside the single images. For the $VV$ polarization states, the ratio in $C_{12}$ decreases to $5 \pm 1\%$ and increases up to $10 \pm 1\%$ in $C_{11}$ and $8 \pm 1\%$ in $C_{22}$. Consequently, the decreasing of the ratio of spatial coincidences between images and its increasing inside single images is clearly the demonstration that a HOM interference occurs for the bi-photon states of high Schmidt number. The sum of the correlations is somewhat smaller than the 25% ratio measured between twin images without the BS, probably because of the losses of the BS.

In order to estimate the coherence length of the bi-photon states we have measured the variation of the relative ratios of total photon-pairs detection events in images as a function of the time delay for $VV$ polarisation states. These relative ratios (Eq. 4) correspond to the ratio of detection of photon-pairs measured between twin images as well as inside single images, divided by the sum of the ratios of detection of photon-pairs without the BS. Results are depicted in Fig. 4. As expected, while a HOM dip is clearly exhibited for correlations between images, a HOM maximum is observed for correlations inside single images. From nonlinear fits, we estimate the visibility of the HOM dip to $30\% \pm 10\%$ which is much smaller than the expected visibility (95%). This large discrepancy is probably due to the cumulated geometric aberrations in the imaging systems and some residual misalignements that tend to blur the interference. However, we would like to emphasize that we achieve the simultaneous two-photon interference of 1500 spatial modes, i.e. two order of magnitude more than in the paper of Lee et al.[15]. From the nonlinear fits of the experimental data depicted by the dotted curves in Fig. 3, we estimate the standard deviation of the gaussian shape of these curves to $\sigma_t = 133.1 \pm 0.2\, fs$ which corresponds to a wavelength standard deviation $\sigma_\lambda = \frac{\lambda_{SPDC}^2}{2\pi c \sigma_t} = 2\, nm$ ($\lambda_{SPDC} = 709\, nm$), in good agreement with the FWHM bandwidth of the interferential filter.

The next experiment consists in measuring the variation of the relative coincidence ratios $R_{12}$ and $R_{11} + R_{22}$ as a function of the angle between the polarization directions of the twin beams, controlled by means of the HWP. These experimental results, depicted in Fig. 5, clearly show the typical modulation of the HOM interference versus the relative polarization directions of the twin photons, with the same visibilities as in Fig. 4.

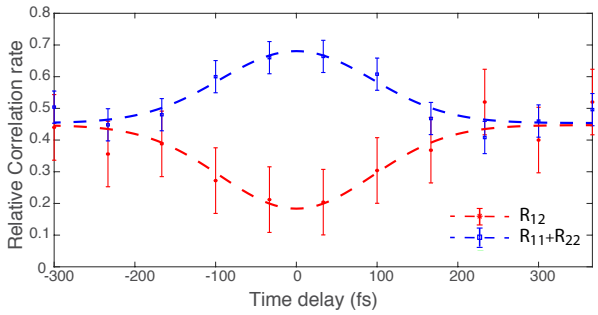


FIG. 4: Relative spatial correlations ratios as a function of the time delay between the two arms of the HOM interferometer when the polarization states of the twin beams are vertical-vertical (VV). The red stars and blue squares correspond to correlations between twin images and inside single images, respectively. The dotted curves correspond to nonlinear fits of the experimental data.

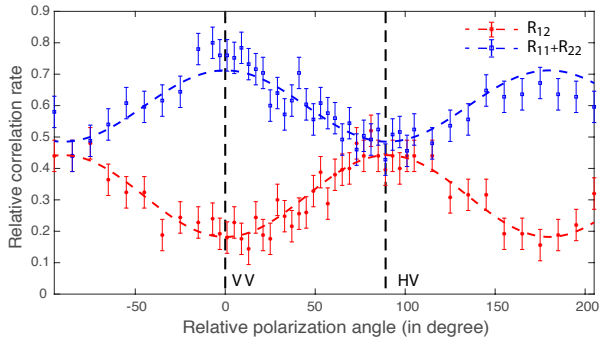


FIG. 5: Correlation ratios as a function of the polarization angle between the two SPDC beams. Red stars and blue squares correspond respectively to correlations between the two images ($R_{12}$) and inside single images ($R_{11} + R_{22}$). The dotted curves correspond to nonlinear fits of the experimental data.

### B. Spatial coherence measurements

To measure the 2D spatial coherence of the bi-photon states, the polarization states of the SPDC beams and the time delay are adjusted to obtain the best polarization and temporal indiscernability of the twin photons. From this initial configuration, vertical and horizontal shifts ($\delta\nu_y$, $\delta\nu_x$) between the reflected and transmitted beams are induced by tilting the BS around its horizontal and vertical axes, respectively (Fig. 1). Then, the variation of the relative spatial correlations ratios between twin images and inside single images is measured as a function of the spatial frequency shifts. These experimental results are given in figures 6 and 7.

In Fig. 6, we present images of the 2D momentum correlations distributions $C_{12}(\Delta\boldsymbol{q})$, $C_{11}(\Delta\boldsymbol{q})$ and $C_{22}(\Delta\boldsymbol{q})$ for three different values of the vertical spatial frequency shift : $\delta\nu_y$ =-4.75, 0 and +3.25 $mm^{-1}$ (Figures 6b to 6j). As it was predicted in [21], single spatial correlation peaks are observed and their positions do not depend on the vertical spatial shift of the reflected beam. Indeed, because of the geometry of the imaging system, vertical shifts of the reflected beams are in opposite directions on each camera (Fig. 2). Consequently, the spatial momentum correlations $C_{12}$ between transmitted-transmitted or reflected-reflected twin photons occur between opposite pixels of the twin images with no shift of the symmetry center. Similarly, the spatial momentum correlations $C_{11}$ and $C_{22}$ between transmitted-reflected or reflected-transmitted twin photons are measured between symmetric pixels along the vertical axis inside single images of both cameras, also with the same symmetry center. In that case, the effect of the vertical shift only results in a variation of the relative total number of spatial coincidences between images and inside single images (Fig. 6a), where $R_{12}$ exhibits a spatial HOM dip and where $R_{11} + R_{22}$ exhibits a HOM peak with the same visibilities as in the temporal domain. From these curves, we estimate the standard deviation of the dip, versus a vertical frequency shift $\delta\nu_y$ induced by the rotation $\delta\phi_{BS}$ of the BS, to $2.7 \pm 0.3$ $mm^{-1}$, which is larger than the standard deviation of the correlation peaks in the far-field images along the vertical direction, i.e. versus the pixel coordinate $\Delta\nu_y$. According to the geometry of the HOM interferometer, while the width of the spatial HOM dip along the vertical direction is limited by the spatial phase matching bandwidth (Eq. 4) for perfect focusing, we have demonstrated in [21] that a small defocusing between image planes quickly reduces the vertical width of the HOM dip.

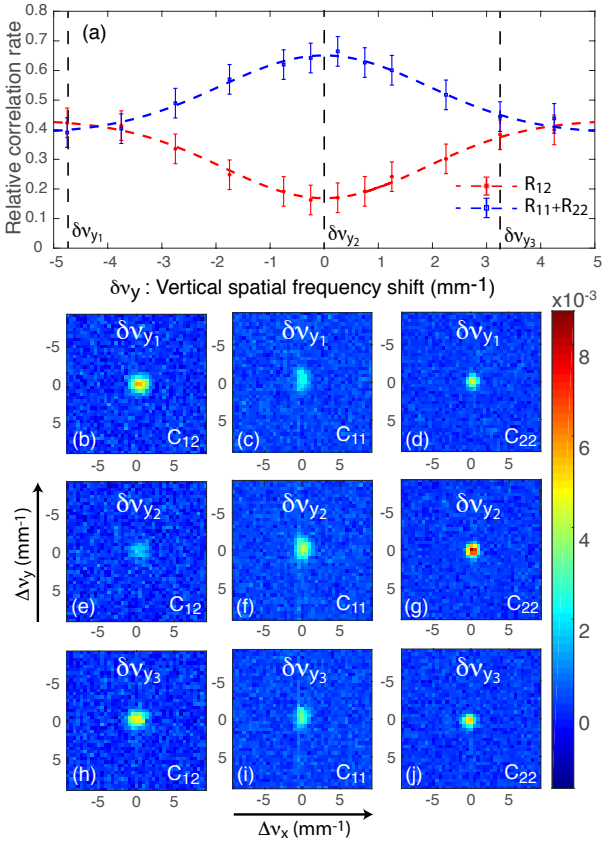


FIG. 6: (a) Relative correlation ratios as a function of the vertical spatial frequency shift $\delta\nu_y$. (b-j) Average normalized spatial momentum correlations distributions $C_{12}$, $C_{11}$ and $C_{22}$ for different values of the vertical shift.

As perfect superposition of the image planes is experimentally difficult to achieve because of the geometric aberrations of the imaging systems, this result is consistent with our previous numerical results.

In Fig. 7, we present the spatial momentum correlation distributions for three different values of the horizontal spatial frequency shift : $\delta\nu_x = \pm 2$ and $0\, mm^{-1}$ (Figures 7b to 7j). Contrary to the results for a vertical shift and in good agreement with [21], the spatial momentum correlations distributions exhibit two correlation peaks centered at $\pm\delta\nu_x$. In $C_{12}$, when $\delta\nu_x \neq 0$, the more intense peak corresponds to the $rr$ twin photons and the other peak corresponds to the $tt$ twin photons. Indeed, the amplitude difference between the two correlations peaks is due to the difference between the reflection and transmission coefficients ($R > T$). Moreover, the distance between the two correlation peaks corresponds to $2\delta\nu_x$. For $C_{11}$ and $C_{22}$, the two correlation peaks are of the same intensity because correlations are calculated between the upper and the lower parts of images where the transmitted and the reflected photons are equally distributed over the area of the detectors. Fig. 7a shows the variation of the relative total number of spatial coincidences between images and inside single images as a function of $\delta\nu_x$ where $R_{12}$ exhibits a spatial HOM dip and where $R_{11} + R_{22}$ exhibits a HOM peak with the same visibilities as in the temporal domain (Fig. 4) and as for a vertical frequency shift (Fig. 6). From these curves we estimate the standard deviations of the dip to $0.7 \pm 0.1$ $mm^{-1}$, in good agreement with the standard deviation of the correlation peak along the horizontal direction.

Finally, we present in Fig. 8 the correlations between the pixels of the two cameras of a given transverse momentum coordinate, for a set of 500 images when the twin beams are spatially and temporally superimposed ($\boldsymbol{\delta q} = \mathbf{0}$, $\delta t = 0$, Fig. 3) and for $HV$ and $VV$ polarisation states. In figures 8c and 8d, we see that the residual correlations between the images for parallel polarizations ($VV$) are localized in some places: the HOM interference is not perfect on the whole image, resulting in the rather low total visibility. Obtaining perfect interference on the whole image deserves further investigation, aiming at reducing the geometric aberrations of the imaging system and eliminating residual misalignements.

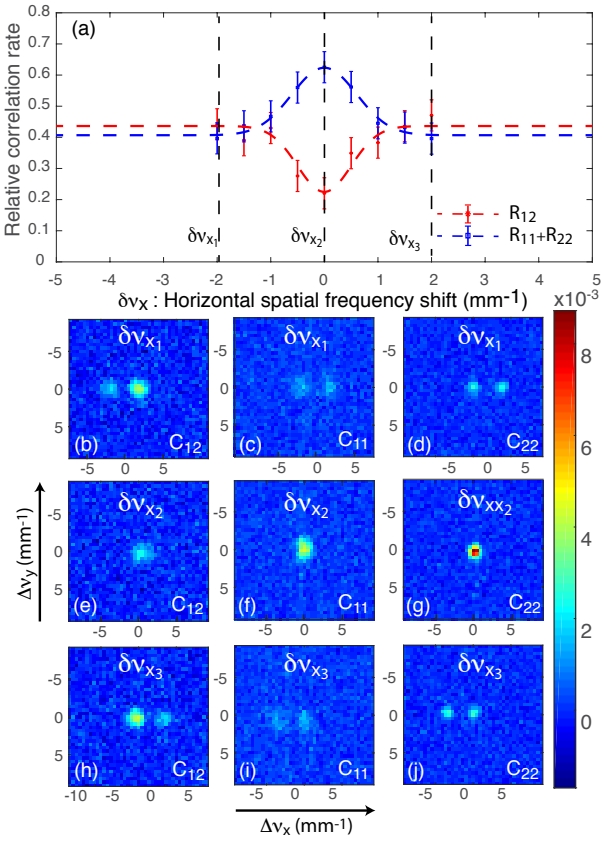


FIG. 7: (a) Relative correlation ratios as a function of the horizontal spatial frequency shift $\delta\nu_x$. (b-j) Average normalized spatial momentum correlations distributions $C_{12}$, $C_{11}$ and $C_{22}$ for different values of the horizontal shift.

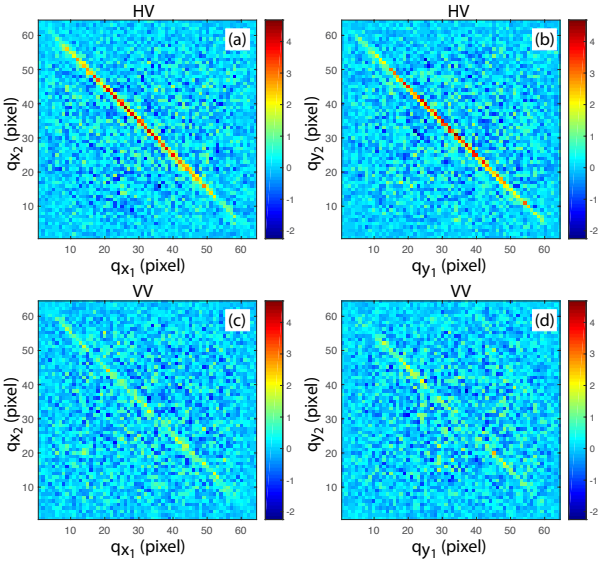


FIG. 8: Correlations between the images for pixels corresponding to a given momentum coordinate $q_x$ ((a) and (c)) or $q_y$ ((b) and (d)), for crossed ((a) and (b)) or parallel ((c) and (d)) polarizations.

## IV. CONCLUSION

We have reported the first experimental observation of fully spatio-temporal HOM interference of bi-photon states of extremely high Schmidt number. Two-photon interference of 1500 spatial modes and more than $3 \times 10^6$ spatio-temporal modes is evidenced by measuring momentum spatial coincidences between pixels of far-field images of two SPDC beams propagating through a HOM interferometer. The output beams are detected with two separate detectors arrays operating in the photon-counting regime. The properties of HOM interference are investigated both in the time and space domains. We show that the two-photon interference exhibits temporal and 2D spatial HOM dips with visibilities of 30% and widths in good agreement with the spatio-temporal coherence properties of the bi-photon states and the geometry of the HOM interferometer. This relatively low visibility is probably due to geometric aberrations of the imaging system. Moreover, we also demonstrate that using detectors arrays, 2D momentum spatial coincidences are resolved between the two output ports as well as inside the two single ports images. This gives access to the rates and the 2D momentum correlations distributions of twin photons detected in pairs between the two cameras and on each camera. We also emphasize that the temporal coherence of the bi-photon states is measured with detectors that record spatial coincidences on the whole set of photons, without a priori selection of the photons in time coincidence.

**Funding**

This work was partly supported by the French "Investissements d'Avenir" program, project ISITE-BFC (contract ANR-15-IDEX-03).

[1] G. Lubin, G. Lubin, R. Tenne, R. Tenne, I. M. Antolovic, I. M. Antolovic, E. Charbon, C. Bruschini, C. Bruschini, D. Oron, et al., Opt. Express, OE **27**, 32863 (2019), ISSN 1094-4087, URL https://www.osapublishing.org/oe/abstract.cfm?uri=oe-27-23-32863.

[2] P.-A. Moreau, E. Toninelli, T. Gregory, and M. J. Padgett, Nature Reviews Physics p. 1 (2019), ISSN 2522-5820, URL https://www.nature.com/articles/s42254-019-0056-0.

[3] P.-A. Moreau, F. Devaux, and E. Lantz, Phys. Rev. Lett. **113**, 160401 (2014), URL https://link.aps.org/doi/10.1103/PhysRevLett.113.160401.

[4] E. Lantz, S. Denis, P.-A. Moreau, and F. Devaux, Opt. Express, OE **23**, 26472 (2015), ISSN 1094-4087, URL https://www.osapublishing.org/oe/abstract.cfm?uri=oe-23-20-26472.

[5] P. A. Morris, R. S. Aspden, J. E. C. Bell, R. W. Boyd, and M. J. Padgett, Nature Communications **6**, 5913 (2015), ISSN 2041-1723, URL https://www.nature.com/articles/ncomms6913.

[6] S. Denis, P.-A. Moreau, F. Devaux, and E. Lantz, J. Opt. **19**, 034002 (2017), ISSN 2040-8986, URL http://stacks.iop.org/2040-8986/19/i=3/a=034002.

[7] H. Defienne, M. Reichert, and J. W. Fleischer, Phys. Rev. Lett. **121**, 233601 (2018), URL https://link.aps.org/doi/10.1103/PhysRevLett.121.233601.

[8] F. Devaux, A. Mosset, F. Bassignot, and E. Lantz, Phys. Rev. A **99**, 033854 (2019), URL https://link.aps.org/doi/10.1103/PhysRevA.99.033854.

[9] G. Brida, M. Genovese, and I. R. Berchera, Nature Photonics **4**, 227 (2010), ISSN 1749-4893, URL https://www.nature.com/articles/nphoton.2010.29.

[10] E. Toninelli, M. P. Edgar, P.-A. Moreau, G. M. Gibson, G. D. Hammond, and M. J. Padgett, Opt. Express, OE **25**, 21826 (2017), ISSN 1094-4087, URL https://www.osapublishing.org/oe/abstract.cfm?uri=oe-25-18-21826.

[11] G. B. Lemos, V. Borish, G. D. Cole, S. Ramelow, R. Lapkiewicz, and A. Zeilinger, Nature **512**, 409 (2014), ISSN 1476-4687, URL https://www.nature.com/articles/nature13586.

[12] C. K. Hong, Z. Y. Ou, and L. Mandel, Phys. Rev. Lett. **59**, 2044 (1987), URL https://link.aps.org/doi/10.1103/PhysRevLett.59.2044.

[13] D. S. Simon, G. Jaeger, and A. V. Sergienko, *Quantum Metrology, Imaging, and Communication*, Quantum Science and Technology (Springer International Publishing, 2017), ISBN 978-3-319-46549-4, URL //www.springer.com/it/book/9783319465494.

[14] Y.-H. Deng, H. Wang, X. Ding, Z.-C. Duan, J. Qin, M.-C. Chen, Y. He, Y.-M. He, J.-P. Li, Y.-H. Li, et al., Phys. Rev. Lett. **123**, 080401 (2019), URL https://link.aps.org/doi/10.1103/PhysRevLett.123.080401.

[15] P. S. K. Lee and M. P. van Exter, Phys. Rev. A **73**, 063827 (2006), URL https://link.aps.org/doi/10.1103/PhysRevA.73.063827.

[16] M. Jachura and R. Chrapkiewicz, Opt. Lett., OL **40**, 1540 (2015), ISSN 1539-4794, URL https://www.osapublishing.org/ol/abstract.cfm?uri=ol-40-7-1540.

[17] R. Chrapkiewicz, M. Jachura, K. Banaszek, and W. Wasilewski, Nature Photon **10**, 576 (2016), ISSN 1749-4893, URL https://www.nature.com/articles/nphoton.2016.129.

[18] Z. Y. Ou and L. Mandel, Phys. Rev. Lett. **62**, 2941 (1989), URL https://link.aps.org/doi/10.1103/PhysRevLett.62.2941.

[19] H. Kim, O. Kwon, W. Kim, and T. Kim, Phys. Rev. A **73**, 023820 (2006), URL https://link.aps.org/doi/10.1103/PhysRevA.73.023820.

[20] S. P. Walborn, A. N. de Oliveira, S. PÃ¡dua, and C. H. Monken, Phys. Rev. Lett. **90**, 143601 (2003), URL https://link.aps.org/doi/10.1103/PhysRevLett.90.143601.

[21] F. Devaux, A. Mosset, and E. Lantz, Phys. Rev. A **100**, 013845 (2019), URL https://link.aps.org/doi/10.1103/PhysRevA.100.013845.

[22] E. Lantz, J.-L. Blanchet, L. Furfaro, and F. Devaux, Mon Not R Astron Soc **386**, 2262 (2008), ISSN 0035-8711, URL https://academic.oup.com/mnras/article/386/4/2262/1466802.

[23] C. K. Law and J. H. Eberly, Phys. Rev. Lett. **92**, 127903 (2004), URL https://link.aps.org/doi/10.1103/PhysRevLett.92.127903.